PHYSICAL REVIEW A **110**, 013114 (2024)

Rydberg-state excitation and ionization of argon atoms subject to elliptically polarized strong laser fields

ZhiQiang Wang,[1,2] Wei Quan,[2,3,*] XiaoLei Hao,[1,†] Jing Chen,[4,5,‡] and XiaoJun Liu[2,3,§]

[1]*Institute of Theoretical Physics and Department of Physics, State Key Laboratory of Quantum Optics and Quantum Optics Devices, Collaborative Innovation Center of Extreme Optics, Shanxi University, Taiyuan 030006, China*

[2]*State Key Laboratory of Magnetic Resonance and Atomic and Molecular Physics, Wuhan Institute of Physics and Mathematics, Innovation Academy for Precision Measurement Science and Technology, Chinese Academy of Sciences, Wuhan 430071, China*

[3]*School of Physical Sciences, University of Chinese Academy of Sciences, Beijing 100049, China*

[4]*Hefei National Research Center for Physical Sciences at the Microscale and School of Physical Sciences, Department of Modern Physics, University of Science and Technology of China, Hefei 230026, China*

[5]*Center for Advanced Material Diagnostic Technology, College of Engineering Physics, Shenzhen Technology University, Shenzhen 518118, China*

(Received 9 April 2024; accepted 1 July 2024; published 16 July 2024)

We experimentally and theoretically investigate the ellipticity dependence of Rydberg state excitation (RSE) and ionization of Ar subject to strong laser fields. It is found that, at 800 nm, the ratio of RSE to ionization yields decreases monotonically with ellipticity for the intensities explored in this work, while, at 400 nm, the ratio decreases monotonically in the high-intensity regime but increases in the low-intensity regime. A dedicated semiclassical model where the influences of Coulomb potential and nonadiabatic effect have been considered can reproduce the experimental observations qualitatively at 800 nm and the high-intensity regime at 400 nm. However, in the low-intensity regime at 400 nm, our semiclassical model cannot reproduce the experimental measurements, indicating that the well-accepted semiclassical frustrated tunneling ionization mechanism is not valid any more for a Keldysh parameter significantly larger than unity. Our work provides a comprehensive understanding of the atomic RSE process and raises a challenge for the theoretical methods in the future.

DOI: 10.1103/PhysRevA.110.013114

I. INTRODUCTION

Rydberg states are atomic or molecular high-lying excited states with energies close to the threshold. These states possess peculiar features, such as large principal quantum number, strong long-range dipole interaction, low ionization energy, etc. These features give rise to its wide applications and significant scientific interests (see, e.g., Refs. [1–3]). Recently, it has been documented that, when atoms or molecules are subject to laser field with strength strong enough for ionization, some of them can even survive in Rydberg states [4,5]. The phenomenon has attracted intensive attention and the relationship between the ionization and excitation dynamics for atoms and molecules subject to strong laser field becomes attractive.

The atomic and molecular ionization dynamics have already been investigated for decades. For an atom subject to a strong laser pulse, an electron can be released via multiphoton ionization (MPI) or tunneling ionization (TI) [6,7]. To identify the transition between these two limits, a significant role is given to the Keldysh parameter $\gamma = \sqrt{I_p/2U_p}$ [8–11], where I_p is the atomic ionization potential and U_p the ponderomotive energy of the laser field. For $\gamma \gg 1$, MPI dominates and the electron may coherently absorb multiple photons. For $\gamma \ll 1$ [7,12], TI becomes important and the features of photoelectron spectra can be largely understood by the classical dynamics. For $\gamma \sim 1$, TI still dominates and the nonadiabatic effect is expected to be important during the tunneling process [13–15]. In the last two regimes mentioned above, after tunneling, the electron wave packet will oscillate along with the laser field and part of the wave packet may return to the parent ion, triggering a wealth of nonlinear physical phenomena, such as high-order harmonic generation [16,17], nonsequential double ionization [18], and high-order above-threshold ionization [19], etc.

In the linearly polarized laser field, it is possible that the return electron does not gain enough drift energy from the laser field and eventually is recaptured to a bound state, leading to the Rydberg state excitation (RSE). This mechanism is dubbed the frustrated tunneling ionization (FTI) [5], which has been widely applied to comprehend the RSE process for atoms [5,20,21], atomic dimers [22], and diatomic molecules [23–25], etc. As documented [5], based on the FTI mechanism, the intensity dependence of both the ionization and excitation yields would be smooth. On the other hand, distinctive out-of-phase oscillations of RSE and ionization yields have been experimentally observed and comprehended by a coherent recapture mechanism [26–28].

---

[*] Contact author: charlywing@wipm.ac.cn

[†] Contact author: xlhao@sxu.edu.cn

[‡] Contact author: chenjing@ustc.edu.cn

[§] Contact author: xjliu@wipm.ac.cn

In addition to the excitation dynamics in a linearly polarized laser field (see, e.g., Refs. [25,29,30]), the RSE process in an elliptically polarized laser field is also of significant interest. Intuitively, the probability of returning to the vicinity of the core for the rescattering wave packet could be lower in the laser field with a larger ellipticity, where the RSE yields are expected to be less. Experimentally, an earlier study is performed by Nubbemeyer *et al.* [5], which shows a dramatic decrease of the RSE yields with ellipticity, as predicted by the FTI mechanism. Theoretically, Landsman *et al.* [31] analyze the ellipticity dependence of RSE yields for He based on the strong-field approximation (SFA) model and argue that the initial transverse momentum of the tunneled electron is compensated by the drift momentum gained in the field, resulting in a peculiar ellipticity dependence of RSE. These calculations well reproduce the experimental data of Nubbermeyer *et al*. [5]. A theoretical work for Ar is reported by Zhao *et al*. [32], where an astonishing maximum of RSE yields at a nonzero ellipticity has been found based on a two-dimensional semiclassical calculation. This interesting phenomenon is inconsistent with a following work by Pauly *et al*. [33], where the calculations are performed by the numerical solution of the time-dependent Schrödinger equation. A more recent work [34] demonstrates that this anomalous behavior will disappear if the nonadiabatic effect is included in a three-dimensional semiclassical model and the absence of this anomalous behavior can partly be attributed to the nonadiabatic corrections of the instantaneous ionization rate and the initial photoelectron momentum distribution at the tunnel exit.

Although the above-mentioned theoretical and experimental endeavours have been made, a consensus on the anomalous ellipticity dependence behavior of the ratio of RSE to ionization yields has not been reached. Apparently, absence of the relevant experimental evidence could be the main obstacle to solving this problem.

In this paper, the ellipticity dependence of RSE and ionization in the laser fields at both 400 and 800 nm is investigated experimentally and theoretically. Our results show that, at 800 nm, the ratio of RSE to ionization yields decreases monotonically with increasing ellipticity for the intensities explored in this work, while at 400 nm, the ratio decreases monotonically in the higher-intensity regime but increases in the lower-intensity regime. A dedicated semiclassical model where the influence of Coulomb potential and nonadiabatic effect have been considered can reproduce the experimental observations qualitatively at 800 nm and in the high-intensity regime at 400 nm. However, in the low-intensity regime at 400 nm, our semiclassical model cannot reproduce the experimental measurements, indicating that the well-accepted semiclassical frustrated tunneling ionization mechanism is not valid any more for a Keldysh parameter significantly larger than unity. Our work provides a comprehensive understanding of the atomic RSE process and raises a challenge for the theoretical methods in the future.

II. EXPERIMENTAL METHOD

Experimentally, 800-nm laser pulses are generated by a commercial Ti:sapphire femtosecond laser system (Legend, Coherent Inc.) with a repetition of 1 kHz. The laser beam at 400 nm is produced by frequency doubling of the fundamental beam with a 500-µm-thick β-barium borate (β-BBO) crystal. The laser pulse energy is precisely controlled with a combination of a broadband achromatic λ /2 plate and a Glan-Taylor Polarizer. The laser polarization can be altered through rotating a quarter-wave plate before the laser beam is focused into the vacuum chamber by a thin lens with a focal length of 15 cm. The pulse duration of the laser beam is about 35 fs at 800 nm, while at 400 nm, the duration is not measured but estimated to be about 70 fs. Before introduced into the spectrometer, the laser beam passes through an optical aperture with a diameter D of 4.0 (5.0) mm for 400 (800) nm to truncate the laser spot (with a diameter of 18 mm) near the focal lens. The peak laser intensity is calibrated by comparing the measured intensity dependence of Ar^+ yields with the calculations by the Ammosov-Delome-Krainov (ADK) model [35,36].

The singly charged ions and Rydberg atoms generated by the femtosecond laser field are measured by a homemade spectrometer (see Ref. [27] for details). In the interaction chamber of the spectrometer, the base pressure is maintained around 3×10^{-6} Pa. Neutral excited atoms (Ar^*) and singly charged ions (Ar^+) produced by the laser field are detected by a position-sensitive microchannel plate (MCP) detector equipped with a delay-line anode (DLD80 RoentDek Handels GmbH). With the specific electric field scheme employed in our spectrometer [27], the Ar Rydberg atoms with the principal quantum numbers of $n \leqslant 75$ can be detected.

III. THEORETICAL METHOD

A. Adiabatic model

In this work, we employ a classical-trajectory Monte Carlo (CTMC) model to study the ellipticity dependence of RSE yields for Ar subject to the elliptically polarized laser fields. In this model, there are two steps for a RSE process: tunneling ionization and classical evolution of the tunneled electron in a combination of the laser field and Coulomb potential of the ion.

The tunneled electron has a Gaussian distribution versus the transverse momentum perpendicular to the instantaneous laser field. The transverse momentum $p_\perp$ is given randomly in the range of $0 < p_\perp < 1.0$ a.u. and the longitudinal momentum $p_\parallel$ is zero. The definitions of $\boldsymbol{p}_\perp$ and $\boldsymbol{p}_\parallel$ are given in a rotating coordinate, which rotates along with the elliptically polarized laser field, as shown in Fig. 1. Each electron orbit is weighted by the ADK ionization rate [35,37].

Because the duration of the laser pulse (35 fs) is too long to observe any carrier envelope phase (CEP) effect, CEP is set to be zero in our calculations. Thus, the laser electric field is given by

$$\mathbf{F}(t) = F_0 f(t)[\cos(\omega t)\hat{\mathbf{z}} + \varepsilon \sin(\omega t)\hat{\mathbf{x}}], \quad (1)$$

where $F_0 = E_0/\sqrt{\varepsilon^2 + 1}$, E_0 is the peak electric field amplitude, ε the ellipticity, $\hat{\mathbf{z}}$ the major axis, and $\hat{\mathbf{x}}$ the minor axis of the polarization ellipse. In our calculation, a trapezoidal

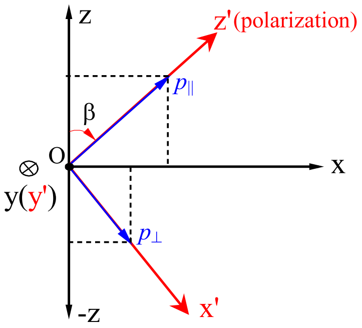

FIG. 1. A graphic illustration of the coordinate systems in the laboratory (x, y, z) and rotating (x', y', z') frames. The red and large (black and small) arrows indicate the coordinate axes of the rotating (laboratory) coordinate system in the polarization plane. The rotating coordinate system rotates along with the laser electric field and z' represents the direction of the transient laser polarization. $\beta = \tan^{-1}[\varepsilon \tan(\omega t_0)]$, where ω is the laser angular frequency and t_0 the instant in question, is the angle between the transient laser polarization direction and the z axis in the x-z plane. $p_\parallel$ ($p_\perp$) indicates the photoelectron initial momentum in the direction of parallel (perpendicular) to the transient laser polarization in the rotating coordinate system.

envelope [38–40] has been applied for the laser field at each wavelength,

$$f_f(t) = \begin{cases} 1, & 0 \leqslant t \leqslant 10T_f \\ \cos^2 \frac{(t-10T_f)\pi}{6T_f}, & 10T_f < t \leqslant 13T_f \\ 0, & t > 13T_f \end{cases} \tag{2}$$

$$f_s(t) = \begin{cases} 1, & 0 \leqslant t \leqslant 20T_s \\ \cos^2 \frac{(t-20T_s)\pi}{12T_s}, & 20T_s < t \leqslant 26T_s, \\ 0, & t > 26T_s \end{cases} \tag{3}$$

where T_f and T_s represent the optical periods of the 800-nm and 400-nm laser fields, respectively. For the intensities explored in this work, our numerical calculations indicate that no significant difference can be identified if the pulse duration of the 400-nm laser beam is increased to 70 fs. After tunneling, the electron evolution in the combined laser field and Coulomb field is obtained from the numerical solution of the classical Newtonian equation, i.e., $\frac{d^2\mathbf{r}}{dt^2} = -\mathbf{F}(t) - \nabla V(r)$, where the effective potential $V(r)$ is given by $V(r) = -\frac{Z_{\text{eff}}}{r}$, $Z_{\text{eff}} = \sqrt{2I_p}$ is the effective charge of the ionic core, I_p is the ionization potential of the atom in question, and r is the distance between the tunneled electron and the parent ionic core. In this adiabatic model, the tunneling exit is given by $\mathbf{r}_0 = -I_p/\mathbf{F}(t_0)$.

We examine the energy E_f of the electron when the laser pulse ends and focus on the electron trajectories with the energies $E_f = \mathbf{P}^2/2 - Z_{\text{eff}}/r < 0$, where $\mathbf{P} = (P_x, P_y, P_z)$ is the final photoelectron momentum. These electrons are captured by the ionic potential, while those with $E_f > 0$ stand for the ionized ones. The weights of the corresponding photoelectron trajectories are summed up to calculate the yields of the RSE and ionization processes, respectively.

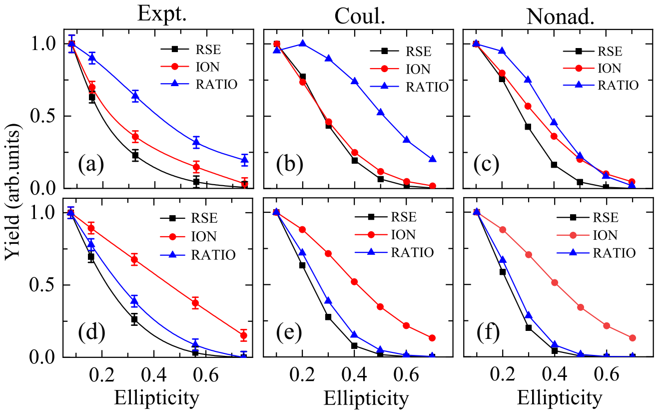

FIG. 2. The measured (a) and (d) and calculated (b), (c), (e), and (f) yields of RSE (black squares), ionization (red circles), and the ratio of RSE to ionization yields (blue triangles) as a function of ellipticity. The data in (b) and (e) are calculated by the semiclassical model where only the influence of Coulomb potential has been considered. The data in (c) and (f) are calculated by the semiclassical model where the influence of Coulomb potential and nonadiabatic effect have been included. The laser intensities are 5.2×10^{13} W/cm^2 for [(a)–(c)] and 1.7×10^{14} W/cm^2 for [(d)–(f)], respectively. The laser wavelength is 800 nm. The measured or calculated data is normalized by the maximum of the corresponding curve.

B. Nonadiabatic model

To describe the ultrafast dynamics more accurately, in our nonadiabatic model, the initial photoelectron momenta, tunnel exit, and instantaneous ionization rate have been further corrected by the nonadiabatic effect [13,34,41–43]. Considering that detailed descriptions on nonadiabatic model have already been given in Ref. [34], only essentials are given here. Based on the S-matrix theory [44,45], the transition probability from the ground state to a continuum state can be described by $W = \exp\{-2\text{Im}S\}$, where $S = \int_{t_s}^{t_0} dt\{\frac{1}{2}[\mathbf{P} + \mathbf{A}(t)]^2 + I_p\}$, $\mathbf{P} = (P_x, P_y, P_z)$ is the final photoelectron momentum after the laser pulse ends in the laboratory coordinate systems, $\mathbf{A}(t)$ is the laser vector potential, and $t_s = t_0 + it_i$ is the complex transition point, which can be obtained from the numerical solution of the saddle-point equation $[\mathbf{P} + \mathbf{A}(\mathbf{t_s})]^2 + 2I_p = 0$. The real part ($t_0$) of t_s is the above-mentioned photoelectron tunneling instant and the imaginary part (t_i) of t_s denotes the imaginary time spent by the electron in the subbarrier process. In our calculations, the tunneling time t_0, the initial photoelectron transverse momentum $\boldsymbol{p}_\perp$, and the initial photoelectron momentum in the y direction $\boldsymbol{p}_{\mathbf{y0}}$ are given randomly in their corresponding parameter spaces. The initial photoelectron longitudinal momentum, t_i, tunnel exit, and instantaneous ionization probability rate can be obtained by solving the saddle-point equation. The following evolution of the photoelectron can be achieved by numerically solving the Newtonian equation $\frac{d^2\mathbf{r}}{dt^2} = -\mathbf{F}(t) - \nabla V(r)$.

IV. RESULTS AND DISCUSSION

The typical experimental results for Ar subject to strong elliptically polarized laser fields at 800 nm are presented in Figs. 2(a) and 2(d). The corresponding Keldysh parameters at $\varepsilon = 0$ are $\gamma = 1.57$ and 0.87, respectively. In Fig. 2(a), the measured ellipticity dependence of RSE, ionization, and the ratio of RSE to ionization yields at 5.2×10^{13} W/cm^2 and 800 nm are presented. The yields of RSE, ionization, and the ratio decrease monotonically with ellipticity. In this work, we also study the ellipticity dependence of the ratio because the ratio is more sensitive to the photoelectron dynamics than the RSE yields. Closer inspection indicates that the decrease of RSE yields with ellipticity is more distinct than that of ionization yields. The laser parameters of Fig. 2(a) are close to those of the data indicated by the blue solid line and open circles in Fig. 1 of Ref. [32], in which an anomalous ratio maximum exhibits around a nonzero ellipticity of $\varepsilon = 0.2$. The result in Fig. 1 of Ref. [32] is in stark contrast to our measurements in Fig. 2(a), where the anomalous ratio maximum at a nonzero ellipticity does not exist.

The difference can be partly attributed to the deficiencies of the two-dimensional adiabatic model employed in Ref. [32]. In the calculations by a two-dimensional adiabatic semiclassical model, we can identify a prominent maximum of the ratio and a less clear maximum of the RSE yields at the nonzero ellipticities, which is qualitatively similar to the result in Ref. [32]. In this two-dimensional model, because the motion of the tunneling electron is confined in the xz plane in the two-dimensional adiabatic model calculation, the electron might possess a higher possibility of coming back to the vicinity of the core if compared to the case of three-dimensional model calculation. Thus, the influence of Coulomb potential could be overestimated in the case of the two-dimensional adiabatic model [34].

The other issue which could give rise to a less pronounced or even absent anomalous ratio maximum at nonzero ellipticity is the influence of the nonadiabatic effect, which can be considered in the nonadiabatic semiclassical model [34]. The calculations by the three-dimensional adiabatic model have been presented in Fig. 2(b), where the ratio maximum appears at the ellipticity of $\varepsilon = 0.2$. These calculation results are apparently inconsistent with the experimental observations in Fig. 2(a). In contrast, as shown in Fig. 2(c), if the nonadiabatic effect has been further considered in the nonadiabatic semiclassical model, the anomalous ratio maximum at nonzero ellipticity disappears and the ratio decreases monotonically with the ellipticity. The nonadiabatic semiclassical model calculations qualitatively match our experimental result, indicating the important role played by the nonadiabatic effect in the regime of $\gamma \sim 1$.

As shown in Fig. 2(d), at a higher laser intensity of 1.7×10^{14} W/cm^2, with rising ellipticity, the ionization yields decay more slowly, while the ellipticity dependence of RSE yields remains almost unchanged if compared to the results in Fig. 2(a). Considering that the Keldysh parameter becomes smaller at a higher intensity, the nonadiabatic effect would become less significant. Indeed, as shown in Fig. 2(f), the calculations by the nonadiabatic model are very close to the calculations by the adiabatic model [see Fig. 2(e)]. Furthermore, both calculations are qualitatively consistent with the experimental measurements.

In order to intuitively comprehend the ellipticity dependence of the ratio of RSE to ionization yields, based on the calculations by the three-dimensional adiabatic CTMC model, we present the tunneling instant (t_0) dependence of the initial photoelectron transverse momentum ($p_\perp$) distributions at $\varepsilon = 0$ and $\varepsilon = 0.2$ for tunneling (including the contributions of both ionization and RSE processes) [Figs. 3(a) and 3(d)], ionization [Figs. 3(b) and 3(e)] and RSE [Figs. 3(c) and 3(f)] at 5.2×10^{13} W/cm^2 and 800 nm. As we can see, the distributions of the RSE are symmetric with respect to $p_\perp = 0$ at $\varepsilon = 0$ and can be roughly divided into three parts, which are indicated by A, B, and C, respectively [see Fig. 3(c)]. With rising ellipticity, regions A, B, and C shift toward the positive direction of $p_\perp$ to compensate the additional acceleration due to the increasing minor axis of the laser field [see Figs. 3(c) and 3(f)]. On the other hand, the tunneling distributions are symmetric with respect to $p_\perp = 0$ [see Figs. 3(a) and 3(d)]. At $\varepsilon = 0.2$, as region A shifts to the momentum around $p_\perp = 0$, where the tunneling probability is the highest [Fig. 3(d)], the yields of region A also become the highest and the distribution of the RSE becomes asymmetric with respect to $p_\perp = 0$ [see Fig. 3(f)]. In the meantime, ionization yields become relatively low [see Fig. 3(e)] because significant tunneling electrons have been recaptured by the Coulomb potential, leaving a prominent groove in the center of the ionization distribution [Fig. 3(e)]. Thus, the ratio of RSE to ionization yields increases with rising ellipticity and reaches a local maximum at $\varepsilon = 0.2$, as shown in Fig. 2(b). As can be comprehended, if the ellipticity increases further, region A will shift away from the peak of tunneling distributions and the ratio starts to decrease.

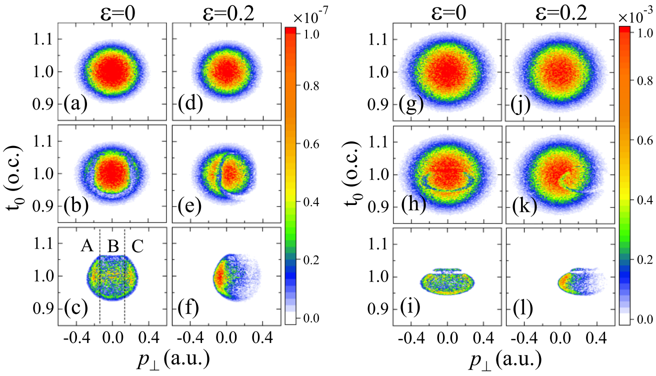

FIG. 3. The tunneling instant (t_0) dependence of the initial photoelectron transverse momentum distribution ($p_\perp$) of tunneling (a, d, g, and j), ionization (b, e, h, and k), and RSE (c, f, i, and l) processes at the ellipticities of $\varepsilon = 0$ [(a)–(c), (g)–(i)], $\varepsilon = 0.2$ [(d)–(f), (j)–(l)]. These data are calculated by the adiabatic model. The laser wavelength is 800 nm. The laser intensities are 5.2×10^{13} W/cm^2 [(a)–(f)] and 1.7×10^{14} W/cm^2 [(g)–(l)], respectively. Please find more details in the text.

To shed more light on the ellipticity dependence of the ratio, the $p_\perp$ distributions as a function of t_0 at a higher intensity of 1.7×10^{14} W/cm^2 are presented in Figs. 3(g)–3(l), where the higher intensity gives rise to wider tunneling distributions along both the t_0 and $p_\perp$ axes. It can be expected that the spatial distributions of photoelectrons have been extended further from the ionic core at a larger intensity after the conclusion of the laser pulse. On the other hand, the Coulomb potential will not vary with the laser intensity. Note that, to be captured by the Coulomb potential, the electrons would appear close to

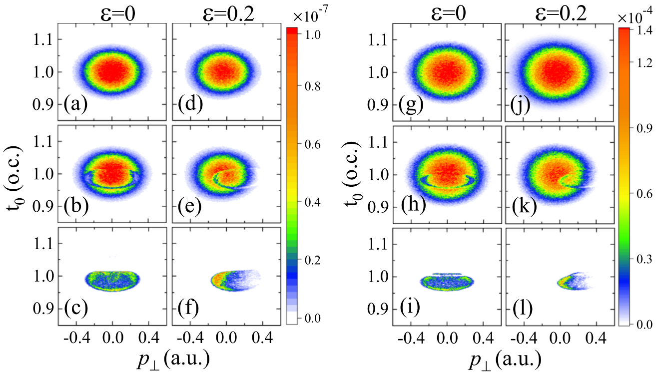

FIG. 4. The tunneling instant (t_0) dependence of the initial photoelectron transverse momentum distribution ($p_\perp$) of tunneling (a, d, g, and j), ionization (b, e, h, and k), and RSE (c, f, i, and l) processes at the ellipticities of $\varepsilon = 0$ [(a)–(c), (g)–(i)], $\varepsilon = 0.2$ [(d)–(f), (j)–(l)]. These data are calculated by the nonadiabatic model. The laser wavelength is 800 nm. The laser intensities are 5.2×10^{13} W/cm^2 [(a)–(f)] and 1.7×10^{14} W/cm^2 [(g)–(l)], respectively. Please find more details in the text.

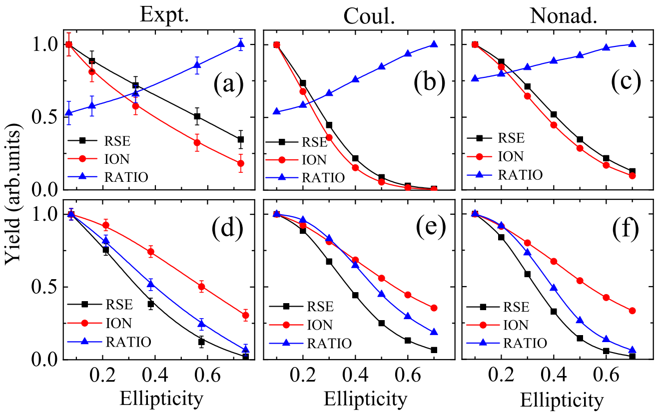

FIG. 5. The measured (a) and (d) and calculated (b), (c), (e), and (f) ellipticity dependence of RSE yield (black squares), ionization yield (red circles), and the ratio of RSE to ionization yields (blue triangles). The data in (b) and (e) are calculated by the semiclassical model where only the influence of Coulomb potential has been considered. The data in (c) and (f) are calculated by the semiclassical model where the influence of Coulomb potential and the nonadiabatic effect have been included. The laser intensities are 3.8×10^{13} W/cm^2 for (a), (b), and (c) and 4.5×10^{14} W/cm^2 for (d), (e), and (f), respectively. The laser wavelength is 400 nm. The measured or calculated result is normalized by the maximum of the corresponding curve.

the core and possess relatively low kinetic energies after the conclusion of the laser pulse. Thus, RSE distributions along the t_0 axis shrink significantly and shift to the negative direction [Figs. 3(i) and 3(l)] because only the electrons born at this area will appear close to the core and obtain relatively low kinetic energies. Because the RSE area shifts lower and shrinks significantly along the t_0 axis with ellipticity and, meanwhile, the tunneling area remains symmetric with respect to $t_0 = 0$, the RSE area will miss the center of the tunneling area, where the yields are highest [see Figs. 3(h) and 3(k)]. In contrast to the lower-intensity case, where a prominent groove appears exactly over the peak of tunneling distributions [Fig. 3(e)] and a local ratio maximum appears at $\varepsilon = 0.2$, at the intensity of 5.2×10^{13} W/cm^2 [Fig. 2(b)], the ratio maximum at $\varepsilon = 0.2$ totally disappears and a monotonous decreasing trend of the ratio at the intensity of 1.7×10^{14} W/cm^2 can be identified in Fig. 2(e). A more detailed analysis can be found in Ref. [34]

In Figs. 4(a)–4(f), the calculations at 5.2×10^{13} W/cm^2 by the nonadiabatic model have been analyzed and presented to comprehend the influence of the nonadiabatic effect. Compared to the calculations by the adiabatic model (see Fig. 3), the nonadiabatic effect gives rise to wider tunneling distributions along the $p_\perp$ axis [see Figs. 4(a) and 4(d)] and narrower RSE distributions along the t_0 axis [see Figs. 4(c) and 4(f)]. Moreover, the RSE distribution shifts toward the negative direction of the t_0 axis, just as the calculations by the adiabatic model at a higher intensity of 1.7×10^{14} W/cm^2. As shown in Figs. 4(b) and 4(e), the RSE distributions miss the most significant part of the tunneling area. Thus, the local ratio maximum at a nonzero ellipticity, which exists only when a groove appears in the center of the ionization distributions, does not exist in Fig. 2(c) and the ratio calculated by the nonadiabatic model at 5.2×10^{13} W/cm^2 declines monotonically with ellipticity [see Fig. 2(c)]. At a higher intensity of 1.7×10^{14} W/cm^2, the tunneling distributions along both $p_\perp$ and t_0 become wider [Figs. 4(g) and 4(j)], while the corresponding RSE distribution at $\varepsilon = 0$ [Fig. 4(i)] is relatively insensitive to the laser intensity. As shown in Fig. 4(l), the RSE distributions shift faster to the positive direction of $p_\perp$ than that in the case of 5.2×10^{13} W/cm^2 [Fig. 4(f)] because a larger $p_\perp$ is necessary to compensate the larger drift momentum gained in the laser field at higher intensity at each ellipticity. Thus, the ratio calculated by the nonadiabatic model at 1.7×10^{14} W/cm^2 declines faster with ellipticity [see Fig. 2(f)] than that in the case of 5.2×10^{13} W/cm^2 [Fig. 2(c)].

The typical measurements on the ellipticity dependence of RSE and ionization for Ar at 400 nm are presented in Figs. 5(a) and 5(d). At the intensity of 4.5 $\times 10^{14}$ W/cm^2 [see Fig. 5(d)], the RSE yields, ionization yields, and the ratio decrease monotonically, with the ellipticity and the RSE yields decreasing the most abruptly. These results are very similar to the case at 800 nm. On the contrary, at the intensity of 3.8×10^{13} W/cm^2 [see Fig. 5(a)], with rising ellipticity, the RSE yields decay so slowly that the ratio increases monotonically. In Figs. 5(b), 5(c), 5(e), and 5(f), the calculations by the adiabatic [Figs. 5(b) and 5(e)] and nonaidabatic [Figs. 5(c) and 5(f)] models are presented. Although the calculations at a higher intensity of 4.5×10^{14} W/cm^2 in Figs. 5(e) and 5(f) are close to each other and qualitatively match the experimental measurements [see Fig. 5(d)], the calculations in both Figs. 5(b) and 5(c) deviate significantly from the measurements in Fig. 5(a). In Fig. 5(b), the RSE and ionization yields decrease much more abruptly than the measurements in Fig. 5(a), while in Fig. 5(c), the ellipticity dependence of RSE yields and ionization yields is very close, giving rise to a ratio hardly dependent on the ellipticity. The measured and calculated ellipticity dependence curves show qualitatively agreement at high intensity but exhibit significant discrepancies at low intensity at 400 nm, indicating that the tunneling ionization picture is not viable any longer in the low-intensity regime at 400 nm.

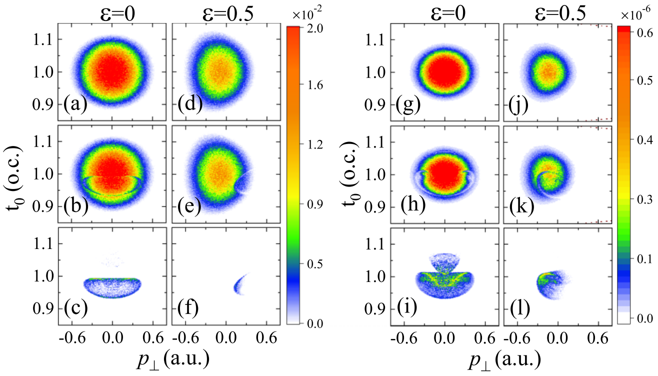

FIG. 6. The tunneling instant (t_0) dependence of the initial photoelectron transverse momentum distributions ($p_\perp$) for tunneling (a, d, g, and j), ionization (b, e, h, and k), and RSE (c, f, i, and l) processes at the ellipticities of $\varepsilon = 0$ [(a)–(c), (g)–(i)] and $\varepsilon = 0.5$ [(d)–(f) and (j)–(l)]. These data are calculated by the nonadiabatic model at laser intensities of 4.5×10^{14} W/cm^2 [(a)–(f)] and 3.8×10^{13} W/cm^2 [(g)–(l)], respectively. The laser wavelength is 400 nm.

To provide more physical insights of the measurements at 400 nm, based on the nonadiabatic model, we calculate the t_0 dependence of $p_\perp$ distributions for tunneling, ionization, and RSE processes at the intensity of 3.8×10^{13} W/cm^2 and 4.5×10^{14} W/cm^2, respectively. The results are given in Fig. 6. In the case of 4.5×10^{14} W/cm^2 [Figs. 6(a)–6(f)], similar to the calculations by the nonadiabatic model at 800 nm [see Figs. 4(c), 4(f), 4(i), and 4(l)], the RSE distributions are narrow along the t_0 axis and shift to the negative direction of t_0 [see Figs. 6(c) and 6(f)]. As expected, the RSE distributions miss the most significant part of the area where the tunneling rate is the highest [see Figs. 6(b) and 6(e)], leading to a monotonically and abruptly decreasing trend of RSE yields with ellipticity. Because the ellipticity dependence of the ionization rate is more gentle compared to the RSE curve at this intensity [Fig. 5(f)], the ratio of RSE to ionization yields still decreases monotonically with respect to the ellipticity. As for the case at 3.8×10^{13} W/cm^2 [Figs. 6(g)–6(l)], the RSE distribution becomes wider along the t_0 axis and another area above $t_0 = 1.0$ o.c. appears at the ellipticity around zero [see Fig. 6(i)]. These enlarged RSE distributions at small ellipticities, which can be mainly attributed to the more important influence of the Coulomb potential in the low-intensity regime at such a short wavelength, give rise to a decreasing trend of RSE yields close to that of ionization yields. Thus, the ratio becomes slowly dependent on the ellipticity.

The significant difference between the calculations by the nonadiabatic model and the measurements at the low-intensity regime and 400 nm indicates that FTI mechanism breaks down. This could be reasonable because the value of the Keldysh parameter ($\gamma = 3.7$) at $\varepsilon = 0$ at the intensity of 3.8×10^{13} W/cm^2 is too large for the FTI mechanism, which is conceived principally based on a semiclassical model [5]. In this intensity and wavelength regime, as documented in our earlier work [27], the RSE process can be understood by the mechanism of the multiphoton resonance with AC-Stark-shifted excited states. Similar results have been documented recently in Ref. [46], where the contributions of RSE based on FTI and multiphoton excitation mechanisms can be controlled by altering the ratio between the strengths of the laser fields at fundamental frequency and second harmonic for a constant intensity of the combined laser field. Nevertheless, the quantitative theoretical calculations on the RSE process at the low-intensity regime and 400 nm are still demanding. Our work raises a challenge for the theoretical methods in the future.

V. CONCLUSION

To conclude, we experimentally and theoretically investigate the ellipticity dependence of the RSE and ionization yields of Ar subject to strong laser fields. Our results indicate that, at 800 nm, the ratio of RSE to ionization yields decreases monotonically with ellipticity for the intensities explored in this work, while at 400 nm, the ratio decreases monotonically in the high-intensity regime but increases in the low-intensity regime. A dedicated semiclassical model where the influence of Coulomb potential and nonadiabatic effect have been considered can reproduce the experimental observations qualitatively at 800 nm and the high intensity at 400 nm. However, in the low-intensity regime at 400 nm, significant deviation between our calculations by the semiclassical model and the measurements can be identified, indicating that the well-accepted semiclassical frustrated tunneling ionization mechanism is not valid anymore for a Keldysh parameter significantly larger than unity. Our work provides a comprehensive understanding of the atomic RSE process and raises a challenge for theoretical methods in the future.

ACKNOWLEDGMENTS

This work is supported by the National Key Research and Development Program (Grant No. 2019YFA0307700), the National Natural Science Foundation of China (Grants No. 12121004 and No. 12274273), the Science and Technology Department of Hubei Province (Grant No. 2020CFA029), and the CAS Project for Young Scientists in Basic Research (Grant No. YSBR-091).

---

[1] M. Saffman, T. G. Walker, and K. Molmer, Rev. Mod. Phys. **82**, 2313 (2010).

[2] J. M. Raimond, M. Brune, and S. Haroche, Rev. Mod. Phys. **73**, 565 (2001).

[3] V. Bendkowsky, B. Butscher, J. Nipper, J. P. Shaffer, R. Löw, and T. Pfau, Nature (London) **458**, 1005 (2009).

[4] W. Bing-Bing, X. F. Li, P. M. Fu, J. Chen, and J. Liu, Chin. Phys. Lett. **23**, 2729 (2006).

[5] T. Nubbemeyer, K. Gorling, A. Saenz, U. Eichmann, and W. Sandner, Phys. Rev. Lett. **101**, 233001 (2008).

[6] D. B. Milošević and F. Ehlotzky, Adv. At. Mol. Opt. Phys. **49**, 373 (2003).

[7] P. Agostini, and L. F. DiMauro, Contemp, Phys. **49**, 179 (2008).

[8] L. Keldysh, Sov. Phys. JETP. **20**, 1307 (1965)

[9] B. Walker, E. Mevel, B. Yang, P. Breger, J. P. Chambaret, A. Antonetti, L. F. DiMauro, and P. Agostini, Phys. Rev. A **48**, R894 (1993).

[10] E. Mevel, P. Breger, R. Trainham, G. Petite, P. Agostini, A. Migus, J. P. Chambaret, and A. Antonetti, Phys. Rev. Lett. **70**, 406 (1993).

[11] J. L. Chaloupka, J. Rudati, R. Lafon, P. Agostini, K. C. Kulander, and L. F. DiMauro, Phys. Rev. Lett. **90**, 033002 (2003).

[12] P. Colosimo, G. Doumy, C. I. Blaga, J. Wheeler, C. Hauri, F. Catoire, J. Tate, R. Chirla, A. M. March, G. G. Paulus, H. G. Muller, P. Agostini, and L. F. DiMauro, Nat. Phys. **4**, 386 (2008).

[13] G. L. Yudin and M. Y. Ivanov, Phys. Rev. A **64**, 013409 (2001).

[14] H. Ni, N. Eicke, C. Ruiz, J. Cai, F. Oppermann, N. I. Shvetsov-Shilovski, and L. W. Pi, Phys. Rev. A **98**, 013411 (2018).

[15] R. Boge, C. Cirelli, A. S. Landsman, S. Heuser, A. Ludwig, J. Maurer, M. Weger, L. Gallmann, and U. Keller, Phys. Rev. Lett. **111**, 103003 (2013).

[16] X. Z. Gao, A. S. Landsman, H. Cao, Y. Zhang, Y. Wang, Y. Fu, and L. W. Pi, Phys. Rev. A **106**, 053105 (2022).

[17] A. D. Shiner, B. E. Schmidt, C. Trallero-Herrero, H. J. Wörner, and S. Patchkovskii, Nat. Phys. **7**, 464 (2011).

[18] W. Becker, X. J. Liu, P. J. Ho, and J. H. Eberly, Rev. Mod. Phys. **84**, 1011 (2012).

[19] G. G. Paulus, W. Nicklich, Huale. Xu, P. Lambropoulos, and H. Walther, Phys. Rev. Lett. **72**, 2851 (1994).

[20] Y. N. Liu, S. P. Xu, M. F. Zhu, Z. R. Xiao, S. G. Yu, L. Q. Hua, X. Y. Lai, W. Quan, W. X. Yang, and X. J. Liu, Chin. Phys. Lett. **40**, 103201 (2023).

[21] J. Zhao, J. Liu, X. Wang, and Z. Zhao, Chin. Phys. Lett. **41**, 013201 (2024).

[22] J. Wu, A. Vredenborg, B. Ulrich, L. Ph. H. Schmidt, M. Meckel, S. Voss, H. Sann, H. Kim, T. Jahnke, and R. Dörner, Phys. Rev. Lett. **107**, 043003 (2011).

[23] A. Emmanouilidou, C. Lazarou, A. Staudte, and U. Eichmann, Phys. Rev. A **85**, 011402(R) (2012).

[24] T. Nubbemeyer, U. Eichmann, and W. Sandner, J. Phys. B **42**, 134010 (2009).

[25] B. Manschwetus, T. Nubbemeyer, K. Gorling, G. Steinmeyer, U. Eichmann, H. Rottke, and W. Sandner, Phys. Rev. Lett. **102**, 113002 (2009).

[26] S. Hu, X. Hao, H. Lv, M. Liu, T. Yang, H. Xu, M. Jin, D. Ding, Q. Li, W. Li, W. Becker, and J. Chen, Opt. Express **27**, 31629 (2019).

[27] S. P. Xu, M. Q. Liu, S. L. Hu, Z. Shu, W. Quan, Z. L. Xiao, Y. Zhou, M. Z. Wei, M. Zhao, R. P. Sun, Y. L. Wang, L. Q. Hua, C. Gong, X. Y. Lai, J. Chen, and X. J. Liu, Phys. Rev. A **102**, 043104 (2020).

[28] S. P. Xu, M. Q. Liu, W. Quan, X. P. Yi, S. L. Hu, L. B. Zheng, Z. Q. Wang, M. Zhao, S. G. Yu, R. P. Sun, Y. L. Wang, L. Q. Hua, X. Y. Lai, W. Becker, J. Chen, and X. J. Liu, Phys. Rev. A **106**, 063106 (2022).

[29] K. N. Shomsky, Z. S. Smith, and S. L. Haan, Phys. Rev. A **79**, 061402(R) (2009).

[30] J. McKenna, S. Zeng, J. J. Hua, A. M. Sayler, M. Zohrabi, Nora G. Johnson, B. Gaire, K. D. Carnes, B. D. Esry, and I. Ben-Itzhak, Phys. Rev. A **84**, 043425 (2011).

[31] A. S. Landsman, A. N. Pfeiffer, C. Hofmann, M. Smolarski, C. Cirelli, and U. Keller, New J. Phys. **15**, 013001 (2013).

[32] Y. Zhao, Y. Zhou, J. Liang, Z. Zeng, Q. Ke, Y. Liu, M. Li, and P. Lu, Opt. Express **27**, 21689 (2019).

[33] T. Pauly, A. Bondy, K. R. Hamilton, N. Douguet, X. M. Tong, D. Chetty, and K. Bartschat, Phys. Rev. A **102**, 013116 (2020).

[34] Z. Wang, W. Quan, X. Hao, J Chen, and X. Liu, Front. Phys. **11**, 1120654 (2023).

[35] M. V. Ammosov, N. B. Delone, and V. P. Krainov, Sov. Phys. JETP **64**, 1191 (1986).

[36] C. L. Wang, X. Y. Lai, Z. L. Hu, Y. J. Chen, W. Quan, H. P. Kang, C. Gong, and X. J. Liu, Phys. Rev. A **90**, 013422 (2014).

[37] A. M. Perelomov, V. S. Popov, and M. V. Terent'ev, Sov. Phys. JETP **24**, 207 (1967).

[38] L. Zhao, J. Dong, H. Lv, T. Yang, Y. Lian, M. Jin, H. Xu, D. Ding, S. Hu, and J. Chen, Phys. Rev. A **94**, 053403 (2016).

[39] P. Ge and Y. Liu, J. Phys. B **50**, 125001 (2017).

[40] L. B. Fu, G. G. Xin, D. F. Ye, and J. Liu, Phys. Rev. Lett. **108**, 103601 (2012).

[41] D. Trabert, N. Anders, S. Brennecke, M. S. Schöffler, T. Jahnke, L. Ph. H. Schmidt, M. Kunitski, M. Lein, R. Dörner, and S. Eckart, Phys. Rev. Lett. **127**, 273201 (2021).

[42] Z. L. Xiao, W. Quan, S. G. Yu, X. Y. Lai, X. J. Liu, Z. R. Wei, and J. Chen, Opt. Express **30**, 14873 (2022).

[43] M. Klaiber, K. Z. Hatsagortsyan, and C. H. Keitel, Phys. Rev. Lett. **114**, 083001 (2015).

[44] W. Becker, F. Grasbon, R. Kopold, D. B. Milošević, G. G. Paulus, and H. Walther, Adv. At. Mol. Opt. Phys. **48**, 35 (2002).

[45] M. Li, M. M. Liu, J. W. Geng, M. Han, X. Sun, Y. Shao, Y. Deng, C. Wu, L. Y. Peng, Q. Gong, and Y. Liu, Phys. Rev. A **95**, 053425 (2017).

[46] W. Zhang, Y. Ma, C. Lu, F. Chen, S. Pan, P. Lu, H. Ni, and J. Wu, Adv. Photonics **5**, 016002 (2023).